Recent Advances in Humanities, Commerce, Management, Engineering, Science & Technology

ISBN: 978-93-94819-13-9
Pub. Date: 30 Sept. 2022
Volume: I

SYNTHESIS, STRUCTURAL, TEXTURAL, OPTICAL, PHOTOLUMINESCENCE AND MAGNETIC PROPERTIES OF HEMATITE (A-FE_2O_3) NANOPARTICLES. EVALUATION OF *IN-VITRO* ANTIOXIDANT AND CYTOTOXICITY ASSAYS

Anjuthaprabha N[1] And Swarnalatha A[2]

[1,2]Assistant Professor, Department of Food Science and Nutrition, Nehru Arts and Science College, Coimbatore-641 105, Tamilnadu, India.

***Corresponding Author*- Anjuthaprabha N**

E-mail: anjuthaprabha@gmail.com

Abstract

We fabricated Hematite (α-Fe_2O_3) nanoparticles from thermal decomposition iron(III)malonatedihydrazinate ([$Fe_2(C_3H_4O_4)_3.2N_2H_4$]) inorganic precursor which was prepared by the co-precipitation method and characterized through EDS, ICP-AES, FT-IR and TG-DTA analysis. To characterize the composition, structural phase, chemical state, morphological, textural, optical, photoluminescence and magnetic properties of fabricated Hematite (α-Fe_2O_3) nanoparticles techniques such as EDS, ICP-AES, XRD, FT-IR, Raman, XPS, SEM, TEM, BET, UV-DRS, PL and VSM were used. In addition, the in-vitro antioxidant activity of Hematite (α-Fe_2O_3) nanoparticles was assessed by DPPH free radical assay and calculated IC50 value found to be 44.52µg/ml. Also, we found the half maximal Inhibitory Concentration (IC50) value of Hematite (α-Fe_2O_3) nanoparticles against MCF-7 cell lines (in-vitro) was found to be 97.6652µg/ml.

Keywords: *Hematite, malonate, hydrazinate, co-precipitation, DPPH, MCF-7.*

Introduction

Hematite (α-Fe_2O_3) nanoparticles are scrutinizing as valuable materials due to their novel characteristics, optical[1], magnetic[2] and electrical properties[3]. Thus, because of these properties among past decades, hematite nanoparticles exhibit spacious applications in various fields like photocatalysis[4], lithium batteries [5], gas sensors[6], solar cells[7], pigments[8], magnetic data storage devices, ferro-fluid technology[9], drug carriers for magnetically guided drug delivery[10] and magnetic resonance imaging (MRI)[11]. According to previous works, to synthesize hematite nanoparticles different methods were used which includes sol gel[12-13], hydrothermal[14-16], electrodeposition[17], Microwave assisted[18-19], electrospinning[20-22], pulsed laser deposition[23-24] and co-precipitation[25-27]. Among these methods, particularly the co-precipitation method paid intensive attention due to its ease of preparation at low temperature and inexpensive nature. Hence, in this work, we used the co-precipitation method to synthesize Hematite (α-Fe_2O_3) nanoparticles from iron(III)adipatedihydrazinate inorganic precursor. From hydrazine derivatives, α-Fe_2O_3 and γ-Fe_2O_3 nanoparticles were prepared earlier[28-29] but there is no information on the iron(III)adipatedihydrazinate inorganic precursor used for synthesizing hematite nanoparticles. Also, herein we report the synthesis of Hematite (α-Fe_2O_3) nanoparticles from thermal decomposition of iron(III)malonatedihydrazinate inorganic precursor prepared via co-precipitation method and then their composition, structural phase, chemical state, morphological, textural, optical, photoluminescence and magnetic properties through their characterization techniques EDS, ICP-AES, IR, Raman, XRD, XPS, SEM, TEM, BET, UV-DRS, PL and VSM. Further, we evaluated *in-vitro* antioxidant and cytotoxicity assay for as-synthesized Hematite (α-Fe_2O_3) nanoparticles.

Experimental

2.1 Synthesis of iron(III)malonatedihydrazinate precursor

ISBN: 978-93-94819-13-9
Pub. Date: 30 Sept. 2022
Volume: I

The analytical grade reagents malonic acid, hydrazine hydrate(99.9% pure and density-1.032 g/ml), ferrous sulphate heptahydrate, concentrated hydrochloric acid, carbon tetrachloride, ethanol and diethyl ether were used. Double distilled water was used throughout in this work. Iron(III)malonatedihydrazinate precursor ($[Fe_2(C_3H_4O_4)_3.2N_2H_4]$) was prepared by the addition of an aqueous solution (50 mL) of hydrazine hydrate (2.0 mL, 0.0399 mol) and malonic acid(3.0g, 0.0212 mol) to the corresponding aqueous solution (50 mL) of ferrous sulphate heptahydrate(2.0g, 0.0071 mol) dropwise with constant stirring. A yellowish brown precipitate formed in a few minutes. The obtained reaction mixture was kept aside for one hour, then filtered, washed with water and ethanol followed by diethyl ether to remove adsorbed impurities and then dried at room temperature. Yield: 6.4 g (90.67%). The general equation for the formation of the iron(III)malonatedihydrazinate precursor may be written as follows :

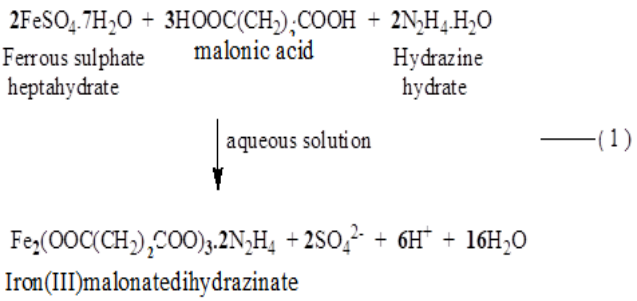

2.2 Synthesis of Hematite (α-Fe_2O_3) nanoparticles

This method involves transferring of the dried iron(III)malonatedihydrazinate inorganic precursor to a silica crucible and calcining in a muffle furnace at 350˚C for 30 minutes resulting in the formation of fine red Hematite (α-Fe_2O_3) nanoparticles (as prepared). The heating source was then removed, the product was allowed to cool to room temperature and then stored in airtight containers.

Characterization techniques

The hydrazine content in the precursor was determined by titration using KIO_3 as titrant under Andrew's conditions[30]. Elemental analysis was performed on an Elementar Vario EL III CHN analyser at digestion temperature in the range of 950-1200˚C. The FT-IR spectra of the solid sample were recorded on an FT-IR spectrophotometer (Shimadzu Prestige-21series) in the spectral range of 4000-400 cm^{-1} using KBr pellets. Differential scanning calorimetry (DSC) measurement of finely powdered sample was performed using a Mettler Toledo DSC 822e. DSC calorimeter at a heating rate of 20°C min^{-1} in the temperature range RT-700 °C. Thermogravimetric (TGA) experiment was carried out using a Perkin Elmer, STA-6000, at a heating rate of 20 °C min^{-1} in the temperature range RT-700 °C. Platinum cups were used as sample holders and alumina as a reference.

ICP-AES of the solid sample was recorded by atomic emission spectrometer (Thermo Electron IRIS INTREPID II XSP DUO). X-ray diffraction (XRD) pattern of the oxide sample was recorded using Schimadzu XRD 6000 diffractometer at room temperature, with the mean Cukα radiation (λ = 1.5418 Å) at a voltage of 40.0 (kV) and a current of 30.0 (mA), between 10° (2θ) and 90°(2θ) with a sampling pitch of 1° in a continuous scan mode and a speed of 10°/min. Raman spectra were recorded by using Bruker RFS 27 with laser source is Nd: YAG 1064 nm. X-ray photoelectron spectroscopy measurement of a product was conducted by using an Omicron ESCA probe spectrometer with monochromatized Al Kα X-rays (1486.6eV). The TEM micrograph of oxide sample was taken using Jeol/JEM 2100 electron microscope at an accelerating voltage of

ISBN: 978-93-94819-13-9
Pub. Date: 30 Sept. 2022
Volume: I

200kV. Scanning electron microscopy (SEM) was performed with a Hitachi Model S-3000H by focusing on nanoparticles to study morphology. BET surface area was performed on Quantachrome autosorb automated gas sorption system. An optical analysis was performed with UV-Vis spectrophotometer (Varian, Cary 5000, spectral range 175-800 nm). Photoluminescence characterization of the oxide sample was carried out by Fluromax-4 spectrometer in which Xenon is used as the source. The magnetic measurement of the oxide sample was performed at room temperature by vibrating sample magnetometer (Lakeshore VSM 7410).

Biological activities

4.1 Appraisement of the in-vitro DPPH activity

The hydrogen donating ability of Hematite (α-Fe_2O_3) nanoparticles was examined in the presence of DPPH stable radical[31]. In the present work, by using some modification in DPPH method[32], we assessed the antioxidant activity of Hematite (α-Fe_2O_3) nanoparticles. 1 mL of 0.3mM DPPH methanol solution was added to 1 mL of different concentration of α-Fe_2O_3 nanoparticles (10, 20 40, 60 80 100µg/mL). The mixture was allowed for sonication to enhance the reaction between insoluble Hematite (α-Fe_2O_3) nanoparticles and the DDPH reagent and kept in the dark at room temperature for 30 minutes and centrifuged, the supernatant was collected and the absorbance values were measured at 517 nm. The methanol solution was used as a blank and DPPH solution (1 mL, 0.3mM) with 1mL methanol served as negative control. Ascorbic acid was taken as the positive control. A control reaction was carried without the test sample. The mean values were obtained from the triplicate analysis. The percentage of inhibition was calculated by comparing the absorbance values of the control and test samples. The capability to scavenge the DPPH radical was calculated using the followed equation.

$$\text{DPPH scavenging activity (\%)} = \left[A_C - A_{\text{test sample}}/A_C\right] \times 100 \quad \text{——(2)}$$

Where A_C was the absorbance of the control reaction and $A_{\text{test sample}}$ was the absorbance in the presence of a test sample. For determining IC_{50} (the amount of samples required to scavenge 50% of DPPH) a similar procedure is adopted with 10, 20, 40, 60, 80, and 100µg/mL of the Hematite (α-Fe_2O_3) nanoparticles and absorbances were recorded after 30 minutes.

4.2 Appraisement of the in-vitro assay for cytotoxicity activity (MTT assay)

The human breast cancer cells (MCF-7) were obtained from National Centre for Cell Science (NCCS), Pune and grown in Eagles Minimum Essential Medium containing 10% fetal bovine serum (FBS). The cell was maintained at 37˚C, 5% CO2, 95% air and 100% relative humidity. Maintenance cultures were passaged weekly, and the culture medium was changed twice a week. The monolayer cells were detached with trypsin-ethylenediaminetetraacetic acid (EDTA) to make single cell suspensions and viable cells were counted using a hemocytometer and diluted with medium containing 5% FBS to give a final density of $1x10^5$ cells/ml. One hundred microliters per well of cell suspension were seeded into 96-well plates at a plating density of 10,000 cells/well and incubated to allow for cell attachment at 37˚C, 5% CO_2, 95% air and 100% relative humidity. After 24 h the cells were treated with serial concentrations of the test samples. They were initially dispersed in phosphate buffered saline by sonication and an aliquot of the sample solution was diluted to twice the desired final maximum test concentration with serum-free medium. Additional four serial dilutions were made to provide a total of five sample concentrations. Aliquots of 100 µl of these different sample dilutions were added to the appropriate wells already containing 100 µl of the medium, resulting in the required final sample concentrations. Following sample addition, the plates were incubated for an additional

ISBN: 978-93-94819-13-9
Pub. Date: 30 Sept. 2022
Volume: I

48 h at 37˚C, 5% CO_2, 95% air and 100% relative humidity. The medium containing without samples were served as control and triplicate were maintained for all concentrations. After 48 h of incubation, 15µl of MTT (5mg/ml) in phosphate buffered saline (PBS) was added to each well and incubated at 37⁰C for 4h. The medium with MTT was then flicked off and the formed formazan crystals were solubilized in 100µl of DMSO and then measured the absorbance at 570 nm using microplate reader. The % cell inhibition was determined using the following formula.

$$\% \text{ Cell inhibition} = \left[100 - Abs_{sample}/Abs_{control}\right] \times 100 \quad \text{——(3)}$$

Nonlinear regression graph was plotted between % Cell inhibition and Log concentration and IC_{50} was determined using GraphPad Prism software[33,34].

Results and discussion

5.1 Characterization of the precursor

5.1.1 Analytical data

The analytical data of iron(III)malonatedihydrazinate inorganic precursor was given in Table 1. The hydrazine content in the precursor was determined by titration using KIO_3 as titrant under Andrew's conditions[30]. The percentage of elements (C, H, N) and metal (Fe) present in the inorganic precursor were analysed by using Elemental analysis (CHN), EDS and ICP-AES techniques. The analytical data of the precursor is found to be good agreement with the proposed composition of the iron(III)malonatedihydrazinate ($[Fe_2(C_6H_8O_4)_3.2N_2H_4]$) inorganic precursor.

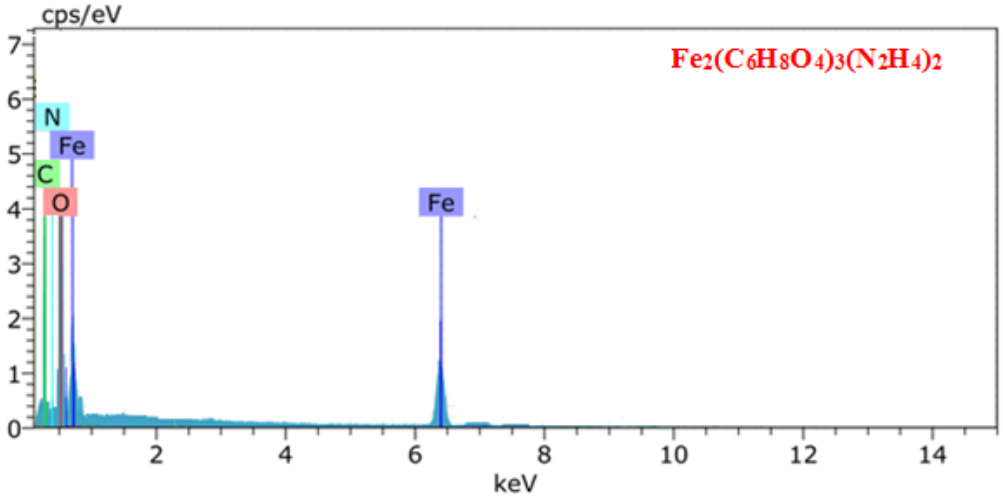

Figure S1. EDS spectra of $[Fe_2(C_6H_8O_4)_3.2N_2H_4]$ precursor.

5.1.2 FT-IR analysis

Investigation of FT-IR spectra of iron(III)malonatedihydrazinate inorganic precursor shows the occurrence of N-H stretching frequency at 3302 cm^{-1}. From the FT-IR spectra, the asymmetric and symmetric carbonyl stretching frequencies at 1612-1550 and1411-1319 cm^{-1} shown by this precursor with an average separation of ($\Delta v = v_{asym} - v_{sym}$) of in the range of 201-231cm^{-1} suggests the unidentate coordination of carboxylate ions to the metal ions. Thus, the adipate dianion coordinates to the metal as the unidentate ligand in the precursor[35]. The N-N stretching frequency appears in the region at 972 cm^{-1} attributes to bridging bidentate nature of hydrazine moieties[36].

ISBN: 978-93-94819-13-9
Pub. Date: 30 Sept. 2022
Volume: I

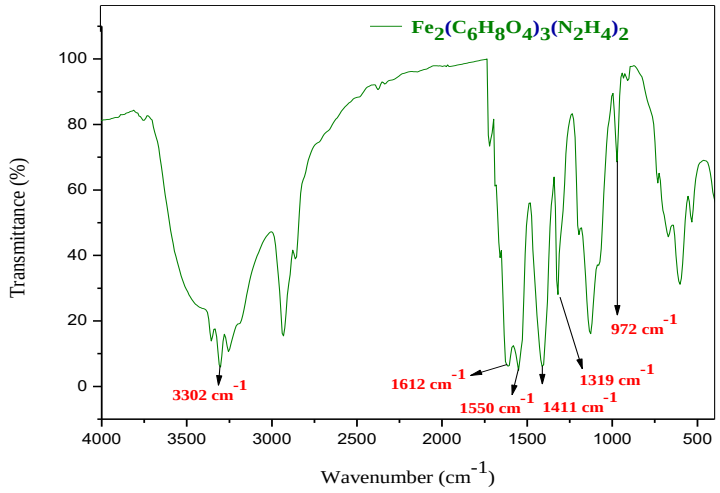

Figure S2. IR spectra of $[Fe_2(C_6H_8O_4)_3.2N_2H_4]$ precursor.

5.1.3 TG-DTA analysis

From TG-DTA, the inorganic precursor $[Fe_2(C_6H_8O_4)_3.2N_2H_4]$ undergoes total weight loss in a single step. The total weight loss of about 80% on the TG curve indicates that the precursor undergoes simultaneous dehydrazination and decarboxylation in a single step observed in the temperature range 300-400°C corresponding DTA peak show the sharp endotherm at 314°C to give fine powders of metal oxide as final residue. Thus, to analyse the products obtained from thermal decomposition of $[Fe_2(C_6H_8O_4)_3.2N_2H_4]$ inorganic precursor by FT-IR, Raman, XRD and XPS analysis, this sample was heated up to 350°C in a muffle furnace in the air atmosphere for 30 minutes.

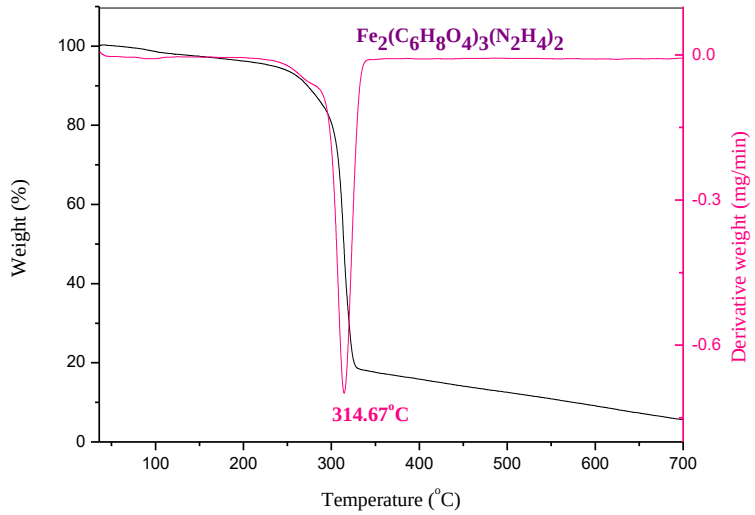

Figure S3. TG-DTA of $[Fe_2(C_6H_8O_4)_3.2N_2H_4]$ precursor.

5.2 Characterization of Hematite (α-Fe_2O_3) nanoparticles

5.2.1 Elemental composition analysis

The presence of elements such as Fe and O in hematite (α-Fe_2O_3) nanoparticles has been analysed by EDS and their compositions have been identified by using ICP-AES analysis. From these findings, no contamination element was detected.

ISBN: 978-93-94819-13-9
Pub. Date: 30 Sept. 2022
Volume: I

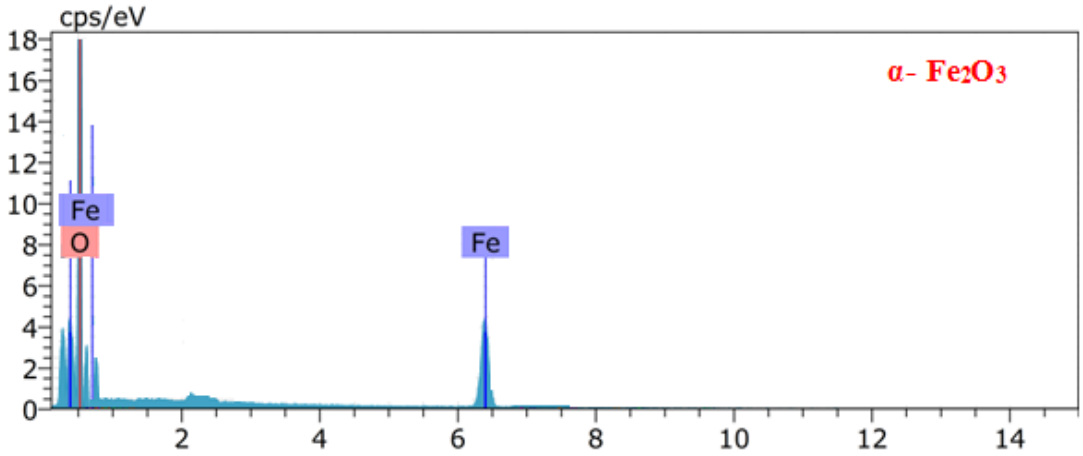

Figure S4. EDS spectra of Hematite (α-Fe_2O_3) nanoparticles.

5.2.2 Structural analysis by X-ray diffraction

Figure 1 shows, the powder X-ray diffraction pattern of α-Fe_2O_3 nanoparticles recorded at room temperature. The XRD pattern of Hematite (α-Fe_2O_3) nanoparticles contains characteristic peaks at 2θ = 24.09°, 33.19°, 35.57°, 40.90°, 43.22°, 49.63°, 54.09°, 57.25°, 62.66°, 64.09°, 72.09° and 75.46° corresponding to the plane orientation (012), (104), (110), (113), (202), (024), (116), (122), (214), (300), (119) and (220) perfectly, matched with the standard reference material JCPDS card number (86-0550). Thus, it can be noticed from the Figure, the XRD pattern of Hematite (α-Fe_2O_3) nanoparticles was indexed to the rhombohedral (hexagonal) structure having $R\bar{3}c$ space group as we expected. By using the Debye-Scherrer formula, $D = K\lambda/\beta\cos\theta$, where θ is Bragg diffraction angle, K is Blank's constant, λ is the wavelength of X-ray radiation (1.54), and β is the full width at half maximum (FWHM) of the peaks at the diffracting angle θ, the average crystallite size calculated was about 23 nm[37].

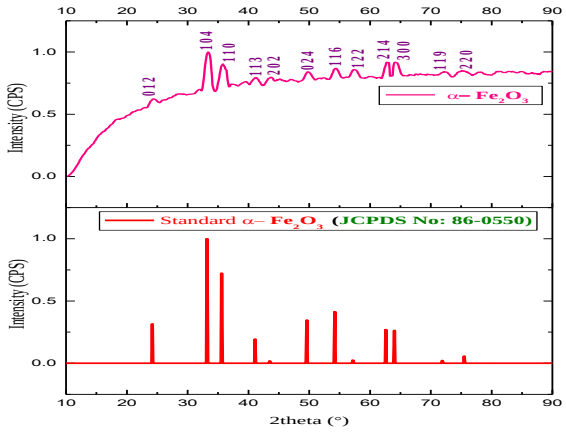

Figure 1. XRD patterns of standard and Hematite (α-Fe_2O_3) nanoparticles.

5.2.3 FT-IR and Raman analysis

FT-IR spectra of Hematite (α-Fe_2O_3) nanoparticles portrays (Figure 2), the occurrence of two absorption bands at 476 and 565 cm^{-1}, implies the formation of Fe-O bond[38,39]. Also, the Hematite (α-Fe_2O_3) nanoparticles were investigated by Raman spectra to identify the phases in it. Figure 3 represents, the peaks at 265.6 and 498.3 cm^{-1} are assigned to A_{1g} phonon modes whereas, the peaks at 245.2, 293.7, 409.1 and 611.4 cm^{-1} are related to E_g phonon modes, which are analogous to earlier reports[40]. In addition, no other iron oxides such as Fe_3O_4 and γ-Fe_2O_3 were detected indicating the purity of the sample. So, the

ISBN: 978-93-94819-13-9
Pub. Date: 30 Sept. 2022
Volume: I

results obtained from XRD, FT-IR and Raman analysis, we confirm the calcined product obtained from iron(III)adipatedihydrazinate precursor is Hematite (α-Fe_2O_3).

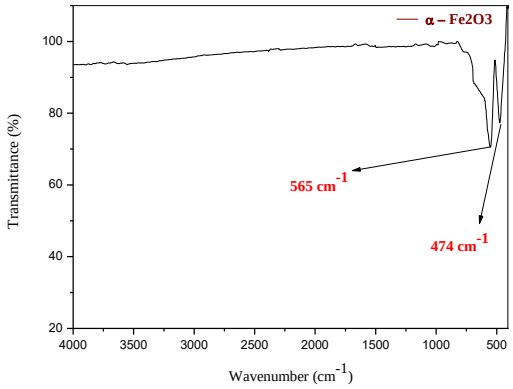

Figure 2. FT-IR spectra of Hematite (α-Fe_2O_3) nanoparticles.

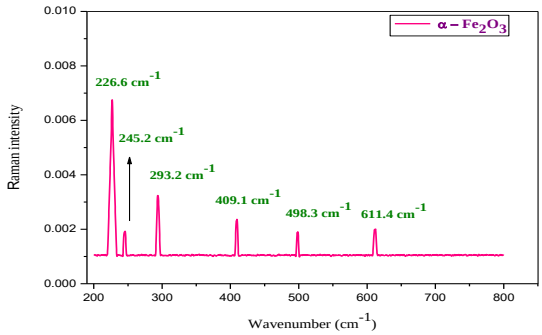

Figure 3. Raman spectra of Hematite (α-Fe_2O_3) nanoparticles.

5.2.4 XPS analysis

To obtain further information about the chemical state and binding energy of Hematite (α-Fe_2O_3) nanoparticles, XPS analysis was performed. Figure 4a-4b depicts, the presence of Fe and O elements. Fe 2p core-level spectra (Figure 4a) states, the two main peaks are located at 711.1 and 724.2 eV, attributed to Fe $2p_{3/2}$ and Fe $2p_{1/2}$ respectively, which are specifically connected with the +3 ionic state of Fe. Along with the two main peaks, two satellite peaks are observed at higher binding energy side (718.2 and 732.7 eV) at about ~8 eV this confirms the presence of only α-Fe_2O_3[13,41] because according to earlier reports Fe_3O_4 does not have satellite peak[42]. Also, the occurrence of Fe^{+3} cations (711.1 eV) rather than Fe^{+2} cations (709 eV) implies the presence of the Fe_2O_3 phase[43]. In addition, previous reports said that XPS spectra for $2p_{3/2}$ of α-Fe_2O_3 have higher binding energy than γ-Fe_2O_3. Thus, in this work, we found that the binding energy of $2p_{3/2}$ of α-Fe_2O_3(711.1 eV) is slightly higher than the binding energy of $2p_{3/2}$ of γ -Fe_2O_3(710.7 eV). Figure 4b demonstrates, one O 1s peak of binding energy at 529.4 eV, which can be ascribed to O^{2-} ions of the lattice oxygen (Fe-O)[13].

ISBN: 978-93-94819-13-9
Pub. Date: 30 Sept. 2022
Volume: I

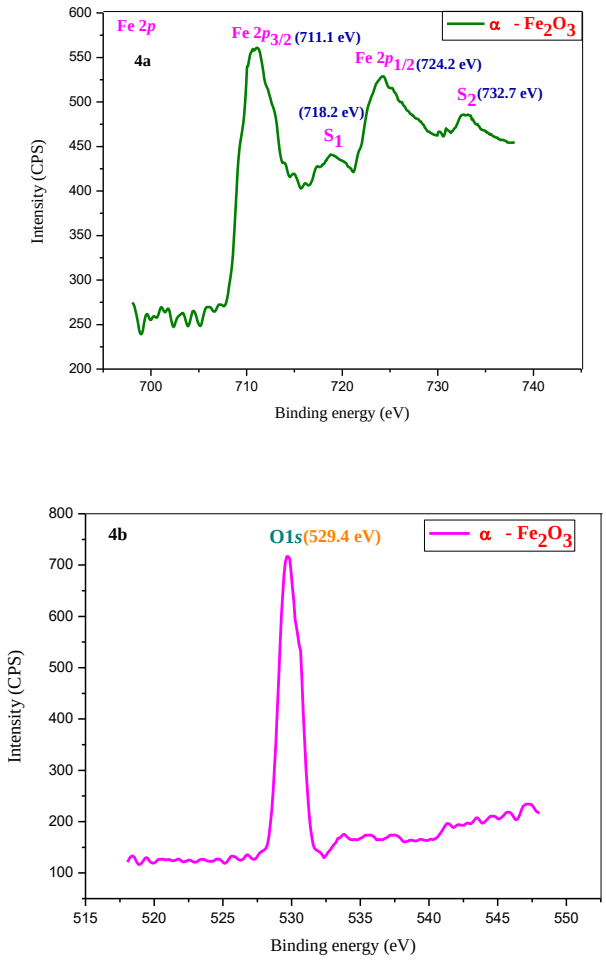

Figure 4. XPS spectra (4a) Fe2*p* and (4b) O1*s* of Hematite (α-Fe_2O_3) nanoparticles.

5.2.5 SEM analysis

SEM picture in Figure 5 of Hematite (α-Fe_2O_3) nanoparticles, clearly showed that the presence of agglomeration in the nanoparticles exhibits irregular spherical-like morphology.

5.2.6 TEM analysis

The TEM micrograph of Hematite (α-Fe_2O_3) nanoparticles is shown in Figure 6, which shows that particles are of spherical shape nanoparticles with the presence of agglomeration. The average particle size was found to be 20-50 nm, which confirms good consistency with the values obtained from XRD.

e2*p* and (4b) O1*s* of Hematite (α-Fe_2O_3) nanoparticles.

ISBN: 978-93-94819-13-9
Pub. Date: 30 Sept. 2022
Volume: I

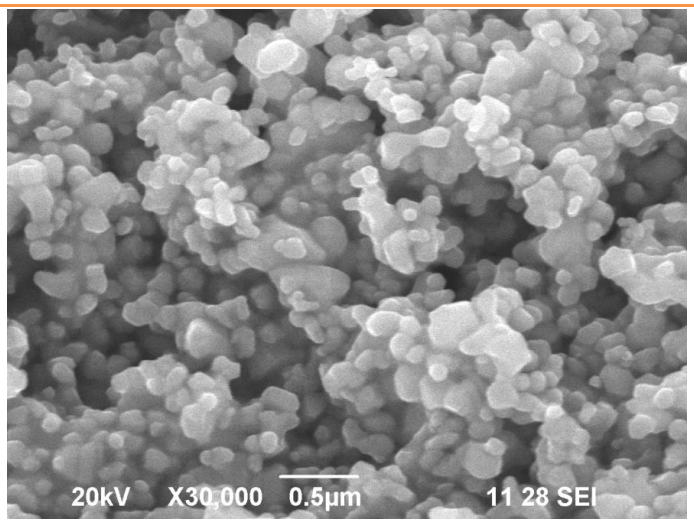

Figure 5. SEM image of Hematite (α-Fe_2O_3) nanoparticles.

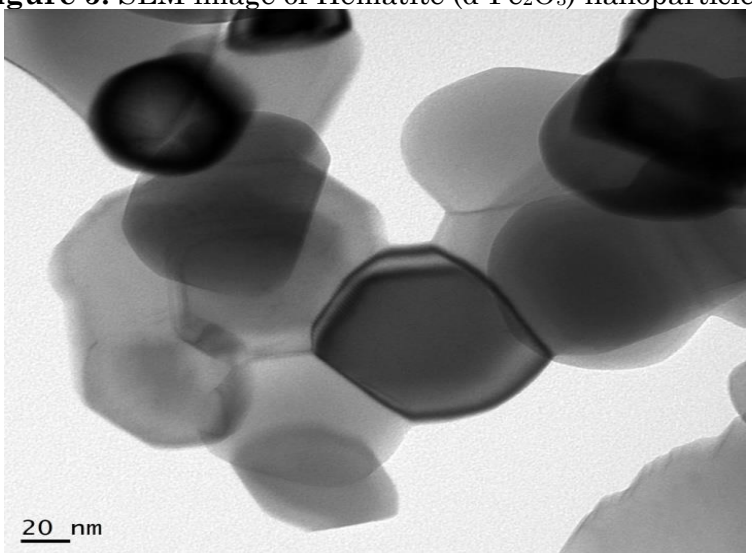

Figure 6. TEM image of Hematite (α-Fe_2O_3) nanoparticles.

5.2.7 Textural analysis

The N_2 adsorption and desorption measurements were performed to estimate the texture properties of Hematite (α-Fe_2O_3) nanoparticles. The isotherm of the samples shown in Figure 7a is not only classified the type IV isotherm with the H3 hysteretic loop in the range of (0.4-1.0)P/P_o but also revealed the presence of aggregated nanoparticles.

The specific surface area for Hematite (α-Fe_2O_3) nanoparticles have been calculated by using the multi-point Brunauer-Emmett-Teller (BET) equation, is 46.818 m^2/g. The approximate average particle size is found to be about 24.4 nm, which is calculated based on the specific surface using the equation, $D_{BET}=6000/(\rho_{\alpha\text{-}Fe2O3}\times S_{BET})$ (in nm), where S_{BET} = specific surface area (m^2/g) and ρ= theoretical density of α-Fe_2O_3 (ρ=5.24 g/cm^3)[45].

From Barrett-Joyner-Halenda (BJH) method, Pore Size Distribution curve (PSD) shown in Figure 7b has been drawn. The PSD curve shows that the pore size at the maximum position is centred at 25.6 nm for Hematite (α-Fe_2O_3) nanoparticles. From the BJH method, the average pore diameter of Hematite (α-Fe_2O_3) nanoparticles is found to be 4.5 nm is calculated by using the relation, $D_p=4V_{BJH}/S_{BJH}$, where V_{BJH}= pore volume (cm^3/g) and S_{BJH} = surface area of pores(m^2/g)[46]. From the above results, there is good consistency with the values observed by XRD, TEM and BET.

ISBN: 978-93-94819-13-9
Pub. Date: 30 Sept. 2022
Volume: I

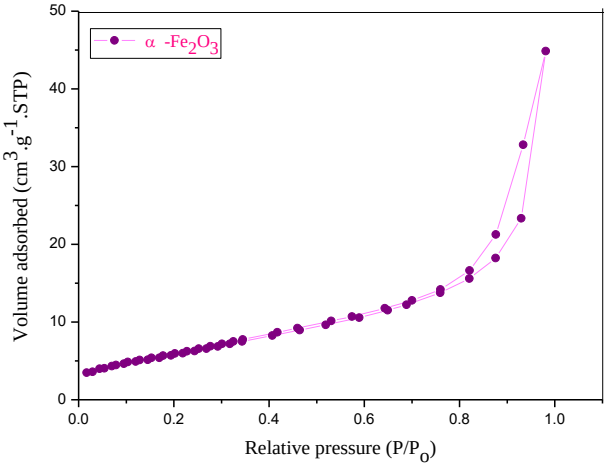

Figure 7a. N_2 adsorption-desorption isotherm of Hematite (α-Fe_2O_3) nanoparticles.

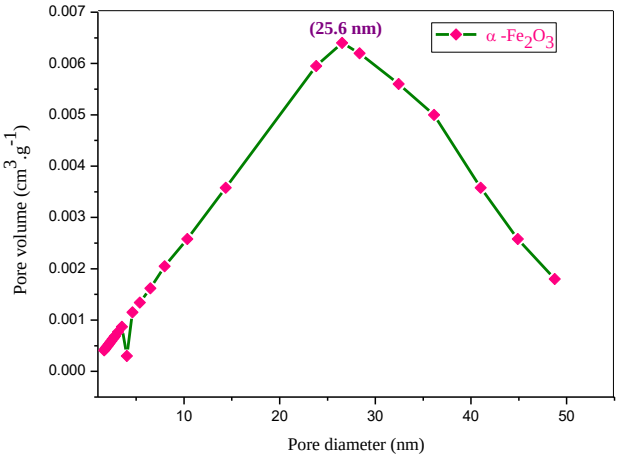

Figure 7b. BJH pore size distribution curve of Hematite (α-Fe_2O_3) nanoparticles.

Optical properties

The UV-Diffuse Reflectance Spectra of absorbance and reflectance (Figure 8a-8b) helps to understand the optical properties of Hematite (α-Fe_2O_3) nanoparticles. As in Figure 8a, Hematite (α-Fe_2O_3) nanoparticles exhibit wide absorption from 250 to 700 nm with maximum absorption in the visible region centred at 434 nm. In Figure 8a, it can be seen that from 250 to 700 nm, Hematite (α-Fe_2O_3) nanoparticles show a very low reflectance which corresponds to high absorbance. Similarly, the region between 700 to 800 nm with low absorbance, shows very high reflectance. By using the following equation, $E_g = 1240/\lambda_{cutt\text{-}off}$, the band gap energy about 1.74 eV was estimated. This value was lesser than the value reported previously[47-48] for Hematite (α-Fe_2O_3) nanoparticles which is due to the quantum confinement effects by the nanosized particles.

Photoluminescence (PL) spectra

The PL emission spectra of the Hematite (α-Fe_2O_3) nanoparticles were measured at room temperature with an excitation wavelength of 434 nm, as shown in Figure 9. It exhibits an intense green emission band centred at 516 nm in the visible region can be observed. Here, this observed green emission results from defects such as oxygen vacancies (based on discussed above XPS O1s spectra of Hematite (α-Fe_2O_3) nanoparticles)[13].

ISBN: 978-93-94819-13-9
Pub. Date: 30 Sept. 2022
Volume: I

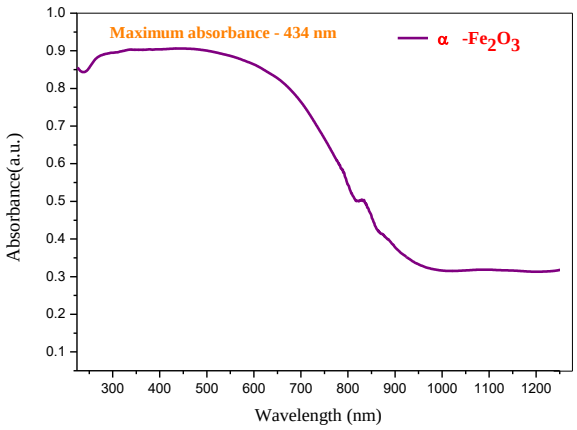

Figure 8a. UV-DRS spectra for absorbance of Hematite (α-Fe_2O_3) nanoparticles.

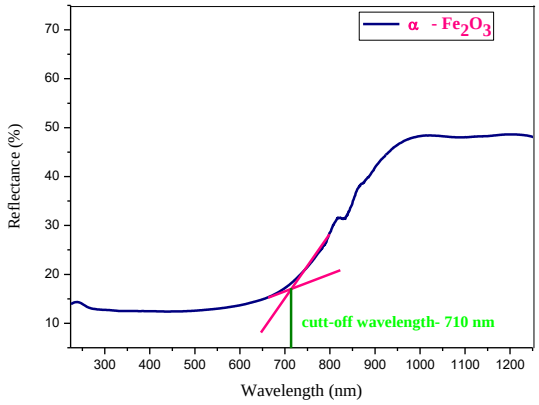

Figure 8b. UV-DRS spectra for Refectance of Hematite (α-Fe_2O_3) nanoparticles.

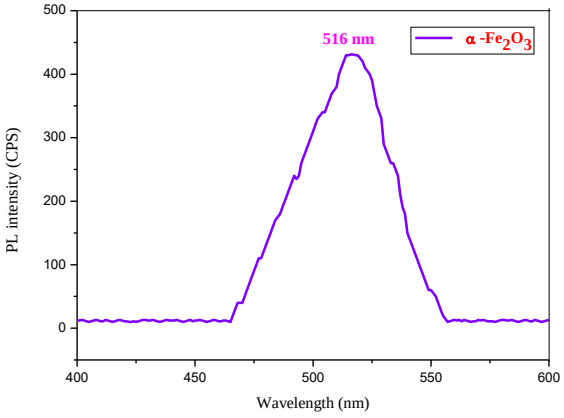

Figure 9. PL spectra of Hematite (α-Fe_2O_3) nanoparticles.

Magnetic Properties

Figure 10 portrays magnetic hysteresis (M-H) loop taken at room temperature with an applied magnetic field in the range of ±20,000 Oe. The magnetic parameters such as saturation magnetization (M_s-1.6942x10^{-3} emu.g^{-1}), retentivity magnetization (M_r-25.828x10^{-6} emu.g^{-1}) coercivity (H_c-81.718 Oe) and squareness (M_r/M_s-0.0152) were observed. Also, the values of anisotropy constant (K_a) of Hematite (α-Fe_2O_3) nanoparticles was calculated as (K_a-0.1412), by using the relation, $K_a=H_cM_s/0.98$, where H_c= coercivity and

ISBN: 978-93-94819-13-9
Pub. Date: 30 Sept. 2022
Volume: I

M_s=saturated magnetization[49]. Similarly, the magnetic moment (μ_m) per unit formula in Bohr magnetron of Hematite (α-Fe_2O_3) nanoparticles was also evaluated as (μ_m-4.844x10^{-5}), by using the relation, $\mu_m=M_sM_w/5585$, where M_s= saturated magnetization, M_w= molecular weight of the sample and 5585= $\beta \times N$ [β is Conversion factor (9.27 × 10−21); N is Avogadro's number][49] . From the above results, the observed low values for magnetic parameters such as M_s, H_c, M_r, M_r/M_s, K_a and μ_m reveals the occurrence of weak ferromagnetism in Hematite (α-Fe_2O_3) nanoparticles.

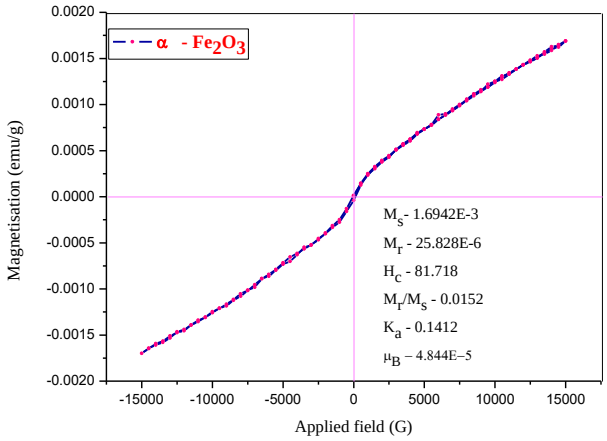

Figure 10. Magnetization(M) *vs* applied field (H) plot of Hematite (α-Fe_2O_3) nanoparticles.

5.3 Biological activities

5.3.1 In-vitro antioxidant activity of Hematite (α-Fe_2O_3) nanoparticles

Figure 11 displays, the DPPH free radical scavenging ability of Hematite (α-Fe_2O_3) nanoparticles with ascorbic acid as standard. The percentage of antioxidant activity of Hematite (α-Fe_2O_3) nanoparticles was assessed by DPPH free radical assay in a dose-dependent manner, because, as the concentration of Hematite (α-Fe_2O_3) nanoparticles increases, the DPPH scavenging activity also increased (Figure 11). But, on comparing the DPPH scavenging activity with standard ascorbic acid, the Hematite (α-Fe_2O_3) nanoparticles exhibit lower scavenging activity but higher than previously reported works[50]. Also, the calculated IC50 value for Hematite (α-Fe_2O_3) nanoparticles (44.52µg/ml) was higher than standard ascorbic acid (24.10µg/ml) but lower than previous works[50]. This result suggests that the Hematite (α-Fe_2O_3) nanoparticles have a very good antioxidant potential which can be used in cytotoxicity and hence in medical treatment.

ISBN: 978-93-94819-13-9
Pub. Date: 30 Sept. 2022
Volume: I

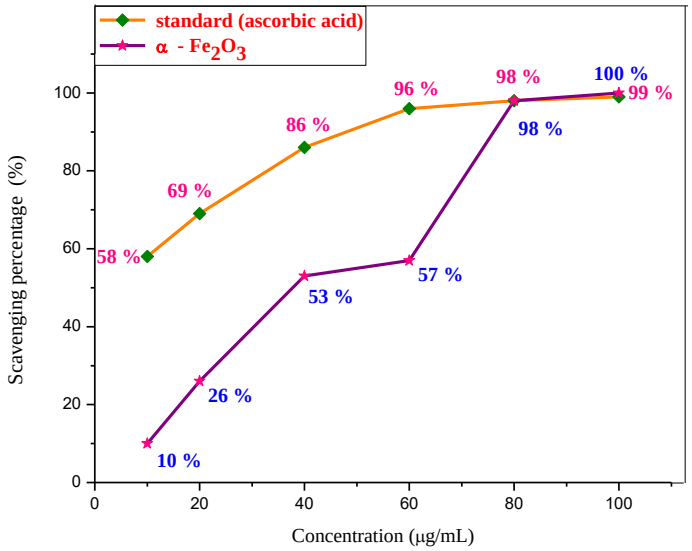

Figure 11. The DPPH scavenging activity of Hematite (α-Fe_2O_3) nanoparticles.

5.3.2 In-vitro cytotoxicity assay of hematite (α -Fe_2O_3) nanoparticles

The cytotoxicity of the Hematite (α-Fe_2O_3) nanoparticles has been investigated against MCF-7 cells via MTT assay. Figure 12 depicts the relative cell viability of cells after they are being treated for 24 h with Hematite (α-Fe_2O_3) nanoparticles with different concentrations ranging from (0.7µg/m-2µg/ml). Controlled samples i.e. untreated samples are also provided for comparison. It has been observed from Figure 12, that the Hematite (α-Fe_2O_3) nanoparticles have inhibited the cancerous cell viability of about 51% at 2µg/ml concentration. Thus, Hematite (α-Fe_2O_3) nanoparticles induced cytotoxicity on MCF-7 cells was found to be increasing with an increase in concentration from 0.7µg/m-2µg/ml. The 50% viability happens at the concentration of 97.66µg/ml which is the half maximal Inhibitory Concentration (IC50). This behaviour of Hematite (α-Fe_2O_3) nanoparticles reveals their dosage-dependent manner like as said in previous reports[51-52]

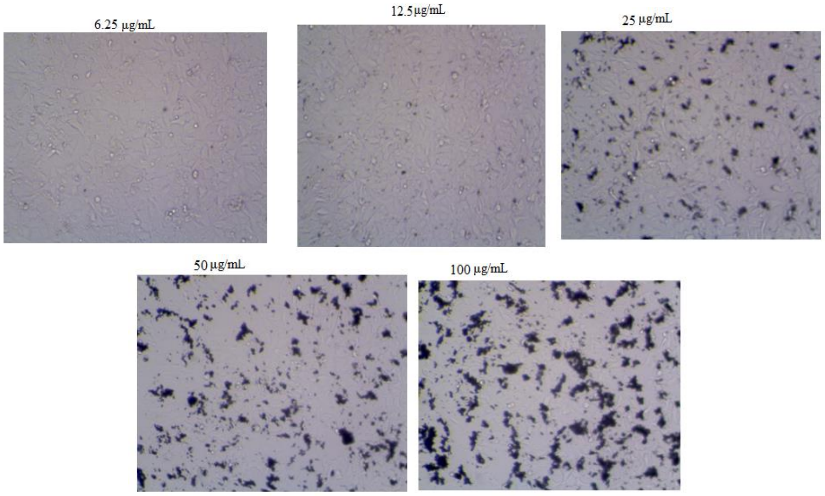

Figure S6. Images of control and different concentrations of Hematite (α-Fe_2O_3) nanoparticles with cells.

ISBN: 978-93-94819-13-9
Pub. Date: 30 Sept. 2022
Volume: I

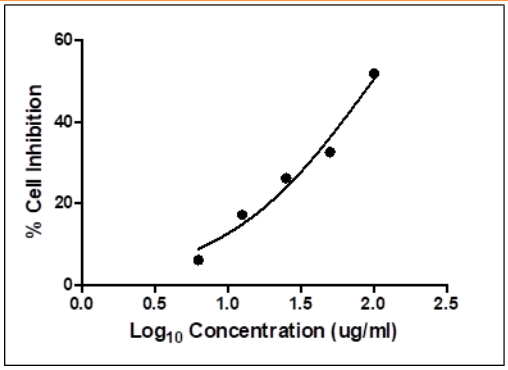

Figure 12. The cytotoxicity of Hematite (α-Fe_2O_3) nanoparticles against MCF-7 cancer cells.

Conclusion

In summary, we have successfully fabricated Hematite (α-Fe_2O_3) nanoparticles via thermal decomposition of an inorganic precursor, Iron(III) malonate dihydrazinate precursor ([$Fe_2(C_6H_8O_4)_3.2N_2H_4$]) which was obtained by a facile co-precipitation method. The inorganic precursor was characterized by EDS, ICP-AES, FT-IR and TG-DTA analysis. The formation of the rhombohedral (hexagonal) structure and purity of Hematite (α-Fe_2O_3) nanoparticles were confirmed by XRD, FT-IR, Raman, EDS and ICP-AES analysis. The oxidation state and binding energy of Hematite (α-Fe_2O_3) nanoparticles were confirmed from XPS analysis. The average particle size of Hematite (α-Fe_2O_3) nanoparticles from XRD is 23 nm which exactly coincides with the results obtained from TEM micrograph.

The SEM image indicated the formation agglomerated Hematite (α-Fe_2O_3) nanoparticles. The specific surface area and pore size distribution of Hematite (α-Fe_2O_3) nanoparticles were estimated from BET and BJH analysis. The optical band gap about 1.74 eV of Hematite (α-Fe_2O_3) nanoparticles was estimated from UV-DRS analysis. PL spectra of Hematite (α-Fe_2O_3) nanoparticles at room temperature revealed emission peak exhibit green emission in the visible region. The weak ferromagnetic behaviour of Hematite (α-Fe_2O_3) nanoparticles was obtained from VSM analysis at room temperature. The in vitro antioxidant and cytotoxicity assays demonstrated that Hematite (α-Fe_2O_3) nanoparticles exhibited significant dose-dependent manner.

Acknowledgement

The authors express their immense thanks to Kondunadu Arts and Science College for providing facilities. Authors are also thankful to P.S.G Arts and Science College (Coimbatore), CIT (Coimbatore), SAIF (Cochin), IIT (Madras), Karunya University (Coimbatore), Amrita Centre for Nanosciences and Molecular Medicine (AIMS, Cochin), BIT university (Bangalore), KMCH college of pharmacy (Coimbatore) for providing instrument facilities and biological analysis.

Disclosure statement

No potential conflict of interest was reported by the authors.

References

1. Wang T, Zhou S, Zhang C, Lian J, Liang Y and Yuan W 2014 Facile synthesis of hematite nanoparticles and nanocubes and their shape-dependent optical properties *New J. Chem*. **38**, 46.
2. Tadic M, Panjan M, Damnjanovic V and Milosevic I 2014 Magnetic properties of hematite (α-Fe_2O_3) nanoparticles prepared by hydrothermal synthesis method *Appl. Surf. Sci.* **320**, 183.
3. Mansour H, Letifi H, Bargougui R, Sonia D A -D, Negulescu B, Cécile A -L, Gadri A and Ammar S 2017 Structural, optical, magnetic and electrical properties of hematite (α-Fe_2O_3) nanoparticles synthesized by two methods: polyol and precipitation *Appl. Phys. A* **123**, 787.
4. Mishra M and Chun D -M 2015 α-Fe_2O_3 as a photocatalytic material: A review *Appl. Catal., A: General* **498**, 126.
5. Dong H, Zhang H, Xu Y and Zhao C 2015 Facile synthesis of α-Fe_2O_3

ISBN: 978-93-94819-13-9
Pub. Date: 30 Sept. 2022
Volume: I

nanoparticles on porous human hair-derived carbon as improved anode materials for lithium ion batteries *J. Power Sources.* **300**, 104.
6. Huang J, Yang M, Gu C, Zhai M, Sun Y and Liu J 2011 Hematite solid and hollow spindles: Selective synthesis and application in gas sensor and photocatalysis *Mater. Res. Bull.* **46**, 1211.
7. Shahpari M, Behjat A, Khajaminian M and Torabi N 2015 The influence of morphology of hematite (α-Fe_2O_3) counter electrodes on the efficiency of dye-sensitized solar cells *Sol. Energy* **119**, 45.
8. Walter D 2006 Characterization of synthetic hydrous hematite pigments *Thermochim. Acta* **445**, 195.
9. Rosensweig R E 1985 *Ferrohydrodynamics*, Cambridge University Press, Cambridge.
10. Zhong L S, Hu J S, Liang H P and Cao A M 2006 Self-assembled 3D flowerlike iron oxide nano-structures and their application in water treatment *Adv. Mater.* **18**, 2426.
11. Jeong U, Teng X, Wang Y, Yang H and Xia Y 2007 Superparamagnetic Colloids: Controlled Synthesis and Niche Applications *Adv. Mater.* **19**, 33.
12. Cui H, Liu Y and Ren W 2013 Structure switch between α-Fe_2O_3, γ-Fe_2O_3 and Fe_3O_4 during the large scale and low temperature sol–gel synthesis of nearly monodispersed iron oxide nanoparticles *Adv. Powder Technol.* **24**, 93.
13. Mathevula L E, Noto L L, Mothudi B M, Chithambo M and Dhlamini M S 2017 Structural and Optical properties of sol-gel derived α-Fe_2O_3 Nanoparticles *J. Lumin.* **192**, 879.
14. Song H J, Sun Y and Jia X H 2015 Hydrothermal synthesis,growth mechanism and gas sensing properties of Zn-doped α-Fe_2O_3 microcubes *Ceram. Int.* **41**, 13224.
15. Freyria F S, Barrera G, Tiberto P , Belluso E, Levy D, Saracco G, Allia P , Garrone E and Bonelli B 2013 Eu-doped α-Fe_2O_3 nanoparticles with modified magnetic properties *J. Solid State Chem.* **201**, 302.
16. Basavaraja S, Balaji D S, Bedre M D, Raghunandan D, Swamy P M P and A Venkataraman 2011 Solvothermal synthesis and characterization of acicular α-Fe_2O_3 Nanoparticles *Bull. Mater. Sci.* **34**, 1313.
17. Liu Y, Yu Y -X and Zhang W -D 2012 Photoelectrochemical properties of Ni-doped Fe_2O_3 thin films prepared by Electrodeposition *Electrochim. Acta* **59**, 121.
18. Liu B -G, Yu Y -T, Peng J -H, Srinivasakannan C, Zhang L -B and Guo S -H 2017 Preparation of microsized hematite powder from ferrous sulfate via microwave calcinations *J. Cent. South Univ.* **24**, 1720.
19. Aivazoglou E, Metaxa E, and Hristoforou E 2018 Microwave-assisted synthesis of iron oxide nanoparticles in biocompatible organic Environment *AIP Adv.* **8**, 048201.
20. Liu C, Shan H, Liu L, Li S and Li H 2014 High sensing properties of Ce-doped α-Fe_2O_3 nanotubes to acetone *Ceram. Int.* **40**, 2395.
21. Chang S, Zou Y, Xu X, Liu L, Liu Z and Liu L 2015 Ultrahigh sensitivity of Nd-doped porous α-Fe_2O_3 nanotubes to acetone *Colloids and Surfaces A: Physicochem. Eng. Aspects* **472**, 63.
22. Shan H, Liu C, Liu L, Li S, Wang L, Zhang X, Bo X and Chi X 2013 Highly sensitive acetone sensors based on La-doped α-Fe_2O_3 nanotubes *Sens. Actuators B Chem.***184**, 243.
23. Thai T M N, Kim S R and Kim H J 2014 Synthesis of α-Fe_2O_3 polymorph thin films via a pulsed laser deposition technique *New Phys. Sae Mulli* **64**, 252.
24. Dadashi S, Poursalehi R and Delavari H 2015 Structural and Optical Properties of Pure Iron and Iron Oxide Nanoparticles Prepared via Pulsed Nd:YAG Laser Ablation in Liquid *Procedia Mater. Sci.* **11**, 722.

ISBN: 978-93-94819-13-9
Pub. Date: 30 Sept. 2022
Volume: I

25. Satheesh R, Vignesh K, Suganthi A and Rajarajan M 2014 Visible light responsive photocatalytic applications of transition metal (M = Cu, Ni and Co) doped α -Fe2O3 nanoparticles *J. Environ. Chem. Eng.* **2**, 1956.
26. Rehana D V, Haleel A K and Rahiman A K 2015 Hydroxy, carboxylic and amino acid functionalized superparamagnetic iron oxide nanoparticles: Synthesis, characterization and *in vitro* anti-cancer studies *J. Chem. Sci.* **127**, 1155.
27. Lassoued A, Dkhil B, Gadri A and Ammar S 2017 Control of the shape and size of iron oxide (α-Fe_2O_3) nanoparticles synthesized through the chemical precipitation method *Results Phys.***7**, 3007.
28. Patil K C 1986 Metal-hydrazine complexes as precursors to oxide materials *Proc. Indian Acad. Sci. (Chem. Sci.).* **6**, 459.
29. Suresh K, Mahesh G V and Patil K C 1989 Preparation of cobalt doped γ-Fe_2O_3 and Mn-Zn ferrites **by** the thermal decomposition of the hydrazine precursors *J. Therm. Anal.* **35**, 1137.
30. Vogel I 1986 *A Textbook of Quantitative Inorganic Analysis* Longman, London.
31. Alam M N, Bristi N J and Rafiquzzaman M 2013 Review on *in vivo* and *in vitro* methods evaluation of antioxidant activity *Saudi Pharm. J.* 21, 143.
32. Serpen A, Capuano E, Fogliano V and Gökmen V 2007 A New Procedure To Measure the Antioxidant Activity of Insoluble Food Components *J. Agric. Food Chem.* **55**, 7676.
33. Mosmann T 1983 Rapid colorimetric assay for cellular growth and survival: application to proliferation and cytotoxicity assays *J. Immunol. Methods* **65**, 55.
34. Monks A, Scudiero D, Skehan P, Shoemaker R, Paull K, Vistica D, Hose C, Langley J, Cronise P, Vaigro W A, Gray G M, Campbell H, Mayo J and Boyd M 1991 Feasibility of high flux anticancer drug screen using a diverse panel of cultured human tumour cell lines *J. Natl. Cancer Inst.* **83**, 757.
35. Sivasankar B N and Govindarajan S 1996 Thermal, spectral and magnetic studies on glycine complexes of cobalt(II), nickel(II) and zinc(II) with hydrazine *J. Therm. Anal.* **46**, 117.
36. Yasodhai S and Govindarajan S 2000 Coordination compounds of some divalent metals with hydrazine and dicarboxylate bridges *Synth. React. Inorg. Met.-Org. Chem.* **30**, 745.
37. Raja K, Jaculine M M, Jose M, Verma S, Prince A A M, Ilangovan K, Sethusankar K and Das S J 2015 Sol–gel synthesis and characterization of α-α-Fe_2O_3 nanoparticles *Superlattices Microstruct.* **86**, 306.
38. Xin Z, Yongan N, Xiangdong M, Yao L and Jiupeng Z 2013 Structural evolution and characteristics of the phase transformations between α-Fe_2O_3, Fe_3O_4 and γ-Fe_2O_3 nanoparticles under reducing and oxidizing atmospheres *Cryst. Eng. Comm.* **15**, 8166.
39. Liu S, Yao K, Fu L -H and Ma M -G 2016 Selective synthesis of Fe_3O_4, γ-Fe_2O_3, and α-Fe_2O_3 using cellulose-based composites as precursors *RSC Adv.* **6**, 2135.
40. De Faria D L A, Silva S V and De Oliveira M T 1997 Raman Microspectroscopy of Some Iron Oxides and Oxyhydroxides *J. Raman Spectrosc.* **28**, 873.
41. Tahir A A, Wijayantha K G U, Sina S -Y, Mazhar M and Kee V M 2009 Nanostructured α-Fe_2O_3 Thin Films for Photoelectrochemical Hydrogen Generation *Chem. Mater.* **21**, 3763.
42. Hawn D D and DeKoven B M 1987 Deconvalution as a Correction for Photoelectron Inelastic Energy Losses in the Core Level XPS Spectra of Iron Oxides *Surf. Interface Anal.* **10**, 63.
43. Bhosale M A, Ummineni D, Sasaki T, Hamaned D N and Bhanage B M 2015 Magnetically separable γ-Fe_2O_3 nanoparticles: An efficient catalyst for acylationof alcohols, phenols, and

ISBN: 978-93-94819-13-9
Pub. Date: 30 Sept. 2022
Volume: I

amines using sonication energy under solvent free condition *J. Mol. Catal. A: Chem*. **404**, 8.
44. Wu G, Tan X, Li G and Hu 2010 Effect of preparation method on the physical and catalytic property of nanocrystalline Fe_2O_3 *J. Alloys Compd.* 504, 371.
45. Ren G, Hu D, Cheng E W, Vargas-Reus M A, Reip P and Allaker R P 2009 Characterisation of copper oxide nanoparticles for antimicrobial applications *Int. J. Antimicrob. Agents* **33**, 587.
46. Herdes C, Santos M A, Medina F and Vega L F 2005 Pore Size Distribution Analysis of Selected Hexagonal Mesoporous Silicas by Grand Canonical Monte Carlo Simulations *Langmuir* **21**, 8733.
47. Mansour H, Radhouane B, Cécile A-L, Abdellatif G, and Salah A 2018 Co-precipitation synthesis and characterization of tin-doped α- Fe_2O_3 nanoparticles with enhanced photocatalytic activities *J. Phys. Chem. Solids* **114**, 1.
48. Maji S K, Mukherjee N, Mondal A and Adhikary B 2012 Synthesis, characterization and photocatalytic activity of α-Fe_2O_3 nanoparticles *Polyhedron* **33**, 145.
49. Anjuthaprabha N and Manimekalai R 2019 Synthesis, textural and magnetic properties of doped and undoped CuO nanoparticles *J. Coord. Chem.*
50. Paul S, Saikia J P, Samdarsh S K and Konwar B K 2009 Investigation of antioxidant property of iron oxide particles by 1'-1'diphenylpicryl-hydrazyle (DPPH) method *J. Magn. Magn. Mater.* **321**, 3621.
51. Rajendran K, Karunagaran V, Mahanty B and Sen S 2015 Biosynthesis of hematite nanoparticles and its cytotoxic effect on HepG2 cancer cells *Int. J. Biol. Macromol.* **74**, 376.
52. Narayanan K B and Han S S 2016 One-Pot Green Synthesis of Hematite (α-Fe_2O_3) Nanoparticles by Ultrasonic Irradiation and Their In Vitro Cytotoxicity on Human Keratinocytes CRL-2310 *J. Clust. Sci.* **27**, 1763.